Mechanical Systems and Signal Processing 196 (2023) 110331

Contents lists available at ScienceDirect

Mechanical Systems and Signal Processing

journal homepage: www.elsevier.com/locate/ymssp

Ultra-Tuning of nonlinear drumhead MEMS resonators by Electro-Thermoelastic buckling

Ali Kanj [a], Paolo Ferrari [a], Arend M. van der Zande [a,b], Alexander F. Vakakis [a], Sameh Tawfick [a,c,*]

[a] Department of Mechanical Science and Engineering, University of Illinois at Urbana-Champaign, Illinois 61801, United States
[b] Materials Research Laboratory, University of Illinois at Urbana-Champaign, Illinois 61801, United States
[c] The Beckman Institute of Advanced Science and Technology, University of Illinois at Urbana-Champaign, Illinois 61801, United States

A B S T R A C T

Nonlinear micro-electro-mechanical systems (MEMS) resonators open new opportunities in sensing and signal manipulation compared to their linear counterparts by enabling frequency tuning and increased bandwidth. Here, we design, fabricate and study drumhead resonators exhibiting strongly nonlinear dynamics and develop a reduced order model (ROM) to capture their response accurately. The resonators undergo electrostatically-mediated thermoelastic buckling, which tunes their natural frequency from 4.7 to 11.3 MHz, a factor of 2.4× tunability. Moreover, the imposed buckling switches the nonlinearity of the resonators between purely stiffening, purely softening, and even softening-to-stiffening. Accessing these exotic dynamics requires precise control of the temperature and the DC electrostatic forces near the resonator's critical-buckling point. To explain the observed tunability, we develop a one-dimensional physics-based ROM that predicts the linear and nonlinear response of the fundamental bending mode of these drumhead resonators. The ROM captures the dynamic effects of the internal stresses resulting from three sources: The residual stresses from the fabrication process, the mismatch in thermal expansion between the constituent layers, and lastly, the applied electrostatic forces. The novel ROM developed in this article not only replicates the observed tunability of linear (within 5.5 % error) and nonlinear responses even near the states of critical buckling but also provides insightful intuition on the interplay among the softening and stiffening, which is invaluable for the precise design of similar devices. This remarkable nonlinear and large tunability of the natural frequency are valuable features for on-chip acoustic devices in broad applications such as signal manipulation, filtering, and MEMS waveguides.

1. Introduction

Currently, micro-electro-mechanical systems (MEMS) resonators are indispensable for radio-frequency (RF) signal processing and filtering [1,2], energy harvesting [3–5], and sensing and actuating [6,7]. In the near future, MEMS resonators could enable megahertz to gigahertz acoustic signals that can couple to photonic [8,9] and electric devices [10,11]. Such coupling is promising for future applications like photonic-phononic memory [12,13], quantum information control [14,15], and integrated circuitry [16,17]. For instance, acoustic waves offer an advantage over optical waves in inducing nonlinear interactions over a large space compared to the optical wavelength [18,19], which enables nonreciprocal behaviors [20,21] even in passive settings [22–24].

Buckled MEMS resonators result from the interplay between compressive stresses and the multi-physics arising at small scales, such as thermoelastic and electromechanical effects. While buckling presents a drawback in traditional structural design, a new paradigm exploits buckling to enable new applications in acoustic metamaterials [25].

For example, electrostatic and electrothermal buckling tunes the natural frequency [26–32] and the geometric nonlinearity [33–41] in micro/nano-resonators. Moreover, buckling amplifies the weak thickness variabilities (<5%) among the unit cells of

* Corresponding author.
E-mail addresses: alimk2@illinois.edu (A. Kanj), tawfick@illinois.edu (S. Tawfick).

https://doi.org/10.1016/j.ymssp.2023.110331
Received 18 September 2022; Received in revised form 20 February 2023; Accepted 26 March 2023
Available online 13 April 2023

phononic waveguides until eventually breaking the stiffness-periodicity of the waveguides, which switches off the acoustic transmission [42].

In this work, we study the effect of buckling on MEMS drumhead plate resonators under different electrostatic and thermal conditions (section II). Such drumhead resonators sustain megahertz-to-gigahertz mechanical vibrations with high quality-factors (high Qs) and optical finesse, two valuable features in mechanical, electrical, and optical applications [43–45]. Moreover, the drumhead resonators offer a larger surface area than beams and cantilevers, facilitating optomechanical interactions [44–46]. Ultimately, the drumhead resonators are conveniently manufacturable via bulk micro/nanofabrication techniques [44,45], while allowing for in-situ structural tunability and actuation via piezoelectric [16,46], electrostatic [38], and thermal control [42]. Therefore, we find the drumhead resonators applied in tunable optical cavities [47] and low-loss nonlinear optomechanical couplers [48].

In this work, we experimentally report that electrostatic control of buckling tunes the natural frequency of micro-drumhead resonators by a factor $> 2.40\times$ from 4.7 to 11.3 MHz (section III). Table 1 and Fig. 1 compare this linear-frequency tunability to the tuning capabilities of micro- and nano-resonators reported in the literature. Table 1 and Fig. 1 demonstrate that this work tuning (of $> 2.40 \times$) surpasses the tuning reported in the literature of drumhead 2D-membranes (i.e., sustaining stretching solely) and drumhead plates (i.e., sustaining stretching and bending). Moreover, this work tuning exceeds the tuning observed in all the clamped–clamped beam works of Table 1, except for those in [33,34]. We conjecture that this work attained this "ultra-tuning" because we exploit the electrostatic tunability by controlling the temperature, which adjusts the interplay between the thermal expansion and fabrication-residual stresses.

As for the nonlinear response, we switch the nonlinearity in the resonator's dynamics from softening to stiffening by

Table 1
Literature overview of tuning mechanical micro- and nano-resonators. Considered tuning methods do not include material and geometric design tuning. We only consider the fundamental modes, the reported experimental results, and frequencies above 10s kHz.

Resonator type	Tuning method	Linear frequency tuning	Nonlinearity tuning/switching	Date, [Reference]
Clamped-clamped beam	Electrostatic	~8.25 to ~ 8.8 MHz (1.07 ×)	Detuning of the stiffening nonlinearity	2006, [33]
		~49 to ~ 60 MHz (1.22 ×)	Switching between softening, softening-to-stiffening, and stiffening	2018, [34]
		~112.5 to ~ 118.3 MHz (1.05 ×)	Detuning of the stiffening nonlinearity	2019, [35]
	Joule heating	3.3 to 15.5 kHz (4.70 ×)	–	2017, [26]
		260 to 410 kHz (1.58 ×)	Switching from stiffening to softening	2017, [36]
	Electrostatic and Joule heating	~20 to ~ 90 kHz (4.50 ×)	–	2016, [27]
Drumhead 2D-membrane	Electrostatic	~75 to ~ 90 MHz (1.20 ×)	–	2014, [28]
		~5 to ~ 8 MHz (1.60 ×)	Detuning of the stiffening nonlinearity	2018, [37]
	Piezoelectric	~8.75 to ~ 9.2 MHz (1.05 ×)	–	2015, [29]
Drumhead plate in a waveguide	Electrostatic	~14.9 to ~ 16.85 MHz (1.13 ×)	Detuning of the stiffening nonlinearity	2018, [38]
	Thermal	~11 to ~ 13.25 MHz (1.20 ×)	–	2021, [42]
Drumhead plate (single resonator)	Air pressure	~0 to ~ 200 kHz	–	2009, [30]
	Electrostatic and thermal	4.7 to 11.3 MHz (2.4 ×)	Switching between softening, softening-to-stiffening, and stiffening	2023, [This work]

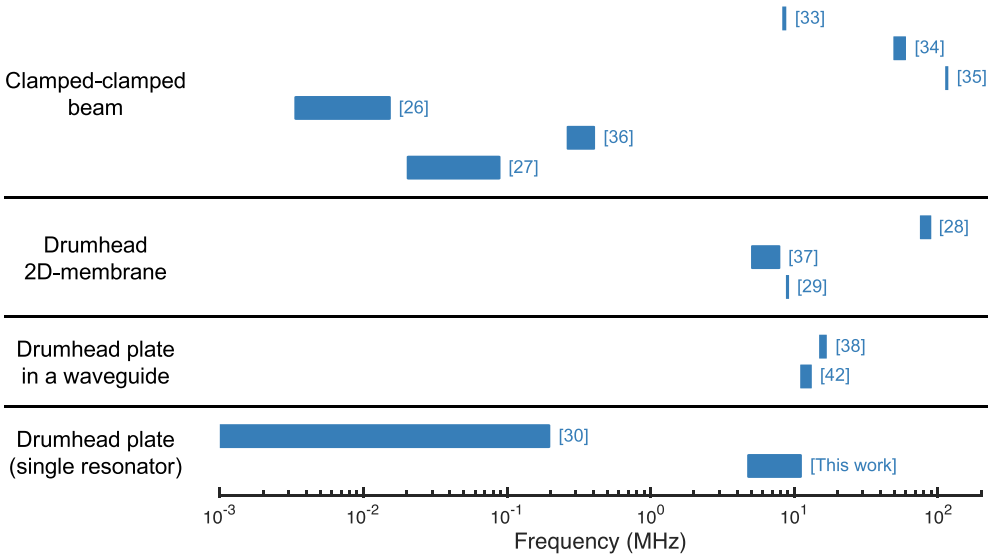

Fig. 1. Graphical representation of the linear frequency tuning achieved in the literature reviewed by Table 1. The left column indicates the resonator type, and each horizontal bar demonstrates the tuning range of the resonators' natural (i.e., linear) frequency on a log scale according to the specified reference to the right of the bar, matching the first and third columns of Table 1, respectively.

electrothermally setting the resonators near the critical buckling, which is the state of minimum natural frequency (section IV). The realized stiffening near-critical buckling covers a broad band of frequencies, thus allowing for a wider operational range [49,50]. The resonators switch from purely softening to purely stiffening by transitioning through a phase of softening-to-stiffening nonlinearity. To the authors' knowledge, this work is the first to report this type of nonlinearity switching in a micro- or nano-drumhead resonator, as illustrated in Table 1. Other drumhead literature accounts for tuning of the stiffening nonlinearity, whereas the nonlinearity switching was only observed in clamped–clamped beams (cf. Table 1).

To explain the observed tunability, we develop a one-dimensional reduced-order model (ROM) that captures the essential mechanisms responsible for buckling in the resonators (section II). The proposed ROM lumps the resonator into a discrete mass. The mass translates along the direction of the bending motion while being subjected to the resonator's bending, stretching, thermal expansion, residual stresses, and the applied voltage on the resonator, which provokes buckling [27,34]. These multi-physical effects are incorporated into the ROM by a discrete electrostatic force and two structural springs. These springs account for the resonator's bending and stretching by assuming an orthogonal configuration that mimics the von Mises truss model of buckling [51]. The free lengths of these springs are temperature-dependent to model the resonator's thermal and fabrication-residual stresses. Therefore, these

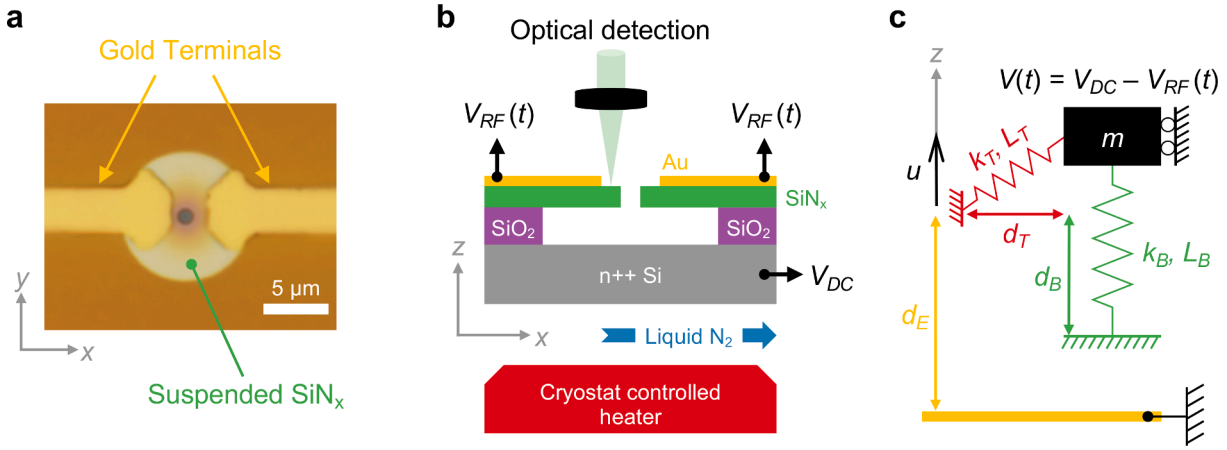

Fig. 2. Design and geometry of the micro-drumhead resonator. (a) Optical microscopic picture of the top view of the drumhead resonator at room temperature with $V_{DC} = 0$ V. The picture shows interferometric coloring (darker orange) at the center of the resonator due to the out-of-plane deflection resulting from buckling. (b) Schematic illustration of the resonator's cross-section passing through the centerline with the gold terminals. The schematic depicts the layered materials, the cryostat temperature control mechanism, the electrostatic actuation, and the optical detection apparatus. (c) Schematic of the reduced-order model (ROM) developed in this work to capture the electrothermal buckling effects on the dynamics of the resonator. (For interpretation of the references to colour in this figure legend, the reader is referred to the web version of this article.)

temperature-dependent springs and the discrete electrostatic force induce compressive effects that buckle the ROM. Remarkably, although relatively simple, the derived discrete ROM predicts very accurately (within 5.5 % error) the experimental tuning in natural frequency for the measured temperatures and electric voltages (section III). The ROM also captures the softening/stiffening switching in the nonlinearity of the response with an accuracy depending on the electrothermal conditions (section IV).

2. Experimental system and reduced-order model

Fig. 2 describes the micro-drumhead resonators and reduced order model we used to study the effect of electrothermal buckling on the dynamics of resonators. Fig. 2a-b show an optical image and schematic of the fabricated micro-drumhead resonators. Each resonator is formed of a $\sim$ 60 nm thick circular silicon nitride (SiN_x) layer of $\sim$ 10.1μ m diameter with a central hole of $\sim$ 1.3μm diameter over a vacuum gap of 150 nm. Patterned 60 nm thick gold electrodes on top of the SiN_x layer allow electrostatic actuation. The underlying silicon is degenerately n++ doped to be conductive and serves as a global electrostatic gate. The SiN_x is initially grown on top of a 150 nm Silicon Dioxide (SiO_2) sacrificial support layer. The SiN_x layer is then released using hydrofluoric (HF) acid, where the central hole allows the HF to access and selectively etch the underlying sacrificial oxide. (cf. supplemental material section S1.a for additional information regarding the fabrication process).

Fig. 2b schematically shows the experimental measurement and tunable electrostatic and thermal controls. The samples are measured inside an optical cryostat, which allows electrical and optical inputs and thermal control. All measurements are performed in a vacuum, with pressure $< 2 \times 10^{-6}$ mBar. We electrostatically actuate the resonators by applying the radio frequency RF voltage $V_{RF}(t) = V_{amp}\sin(\Omega t)$ to the electrodes and a DC voltage V_{DC} to the underlying silicon back gate, leading to a static out-of-plane force F_{DC} (cf. (14)) which tunes the resonator's internal stresses and an RF force F_{RF} (cf. (15)) which drives the resonator to resonate, discussed later as part of the reduced order model. To detect the motion, we focus a laser near the center of the resonator and measure the time-varying reflected light using a photodiode attached to a network analyzer. The resonator is partially transparent, so the light reflecting from the back-gate and the resonator's surface interferes due to Fabry-Perot Interferometry. As a result, the change in reflected light intensity is proportional to the amplitude of motion.

To unravel the relative contributions from electrostatic tuning and the resonator's internal stress, we independently control the internal stress by adjusting the temperature in the optical cryostat. This temperature-change tunes the internal stress in the resonator by the thermal expansions/contractions induced within the structural constraints. As shown in Supplementary Figure S1, when under compression, induced thermal stresses cause the resonator to buckle and deflect out of the plane, creating interferometry fringes depending on their buckled profile. We should note that the interplay between these thermoelastic effects and the fabrication-induced residual stresses define the internal stress (both tensile and compressive) for each temperature. Since the residual stresses are fixed in our experiments, we control the temperature to vary the internal stress.

Before discussing experimental results, we illustrate each of these multi-physics phenomena (i.e., electrostatic force, thermal stresses, and fabrication-induced residual stresses) using the reduced-order model (ROM). Fig. 2c shows the ROM along with the relations of all its constitutive elements. The proposed ROM lumps the drumhead resonator into a discrete mass m. As shown by the rollers in Fig. 2c, the mass m translates with a displacement coordinate u in the z-direction along which the flexural vibrations of the resonator occur while being subjected to the resonator's bending, stretching, thermal expansion, residual stresses, and the applied voltage on the resonator, which provokes buckling [52,34,27,42]. Our ROM captures all these multi-physics effects in the form of discrete springs and forces connected and applied to the translating mass. The configuration of the springs in the ROM is inspired by the von Mises truss model of bistable buckling phenomena [51] by attaching a stretching spring orthogonally to the bending direction.

In addition, the ROM considers the thermal and fabrication-residual stresses by imposing temperature-dependent compressions in the assumed springs. Specifically, the ROM lumps the effective inertia of the resonator into a rigid mass. Therefore, the mass m represents the effective mass of the resonator during its fundamental mode of vibrations, which constitutes the mode of interest for this ROM. The ROM captures the bending and stretching of the resonator by the springs of stiffnesses, k_B and k_T, respectively. The bending spring k_B aligns with the z-direction whereas the stretching spring k_T elongates diagonally with the translation of m. For example, in the absence of all forces and springs in the ROM other than the stretching spring, the zero-equilibrium position (i.e., $u = 0$ m) will be unstable if the stretching spring k_T is compressed to fit within the distance d_T. In this case, m snaps from this unstable zero-equilibrium position to another stable equilibrium position whose location depends on the amount of precompression in the stretching spring k_T. Hence, it is important to quantify the value of precompression in the stretching spring, which we do in the ROM by defining the parameter δ_T as,

$$\delta_T \overset{\text{def}}{=} \frac{L_T - d_T}{d_T}, \tag{1}$$

where L_T is the free length of the stretching spring that is confined within the distance d_T. Under the single effect of the stretching force (cf. supplemental material section S3), the mass m attains the stable equilibrium u_{EQM} approximated to $\mathscr{O}\left[\left(\frac{u_{EQM}}{d_T}\right)^{\frac{3}{2}}\right]$ by:

$$\begin{cases} u_{EQM} = 0 \text{ for } \delta_T \leq 0 \text{ (i.e., spring } k_T \text{ is under pretension)} \\ u_{EQM} = \pm d_T\sqrt{\dfrac{2\delta_T}{1+\delta_T}} \text{ for } \delta_T > 0 \left(\text{i.e., spring } k_T \text{ is under precompression}\right) \end{cases}. \tag{2}$$

Equation (2) shows that δ_T determines the stable equilibrium of mass m, which represents the in-plane strains in the resonator as defined in (1). These in-plane strains result during the fabrication process and by thermoelastic deformation of the resonator; therefore, δ_T depends on the fabrication-residual strains and the resonator's temperature. However, the fabrication and thermal strains do not only affect the in-plane strains in the resonator but also lead to mismatches in deformations/strains between the different material layers that anchor and form the resonator (cf. Fig. 2b). These strain mismatches, especially between the layers of material around the anchoring boundary of the resonator, induce moments that bend the resonator in the transverse z-direction of Fig. 2.

To account for the bending effect of the strain mismatches, we characterize the bending spring k_B in the ROM with the parameter,

$$\delta_B \overset{\text{def}}{=} \frac{L_B - d_B}{d_B}, \tag{3}$$

where L_B corresponds to its free-length and d_B corresponds to the distance confining the bending spring when $u = 0$ m as shown in Fig. 2c. Like δ_T, δ_B depends on the fabrication-residual strains and the temperature T of the resonator. We determine these temperature dependences of $\delta_T(T)$ and $\delta_B(T)$ using experimental measurements that we run at different temperatures controlled by the cryostat depicted in Fig. 2b. Based on these experiments (cf. supplemental material section S4.a and Fig. S14a-b) and literature models [53], we find that δ_T and δ_B scale with temperature T as,

$$\delta_T(T) = \theta_0 + \theta_1 T, \tag{4a}$$

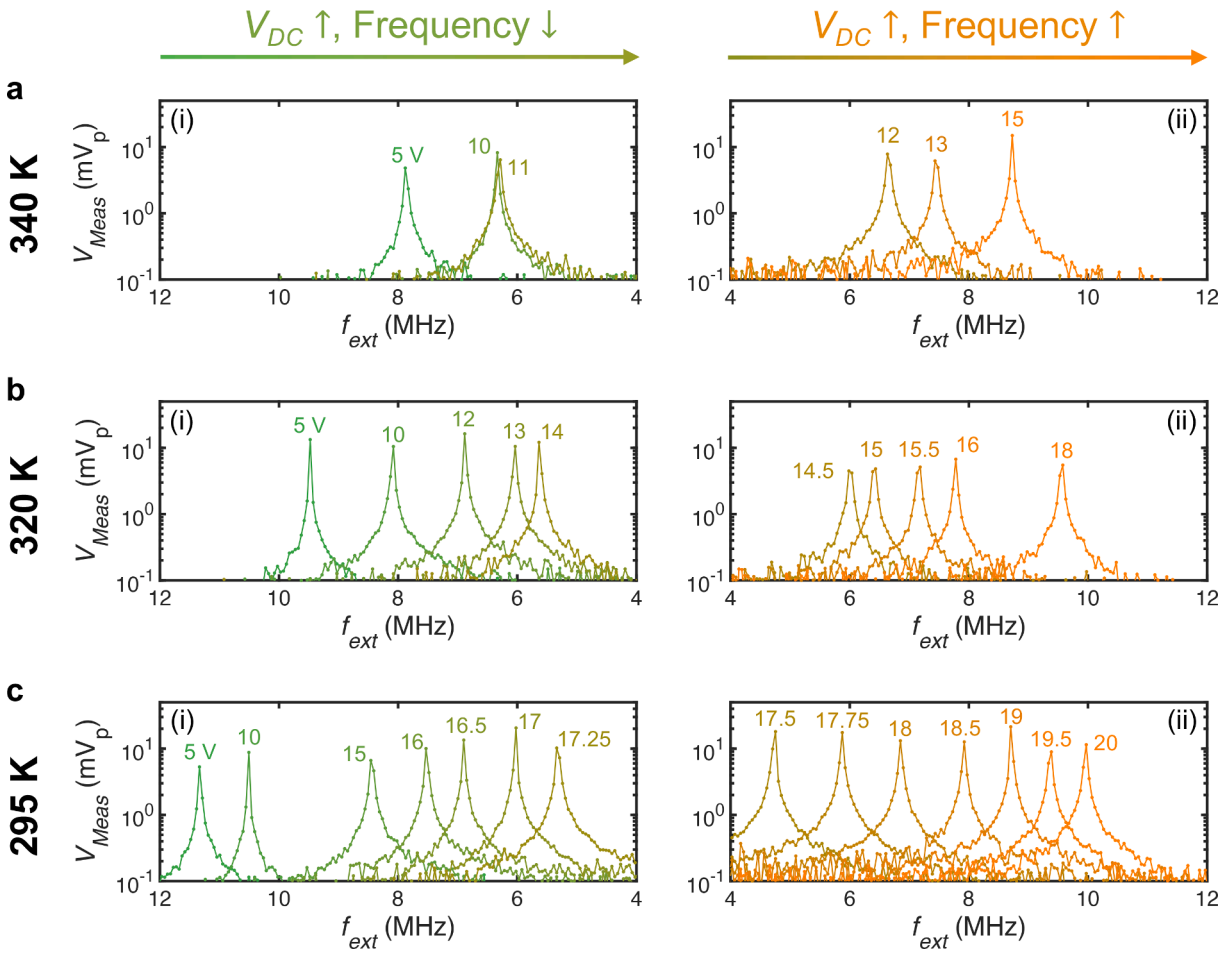

Fig. 3. Electrostatic and thermoelastic tunability of the resonator's linear dynamic response. Experimentally measured frequency response of the resonator at a temperature of (a) 340 K, (b) 320 K, and (c) 295 K for increasing V_{DC} whose values label the respective respoonse. For each temperature in Fig. 3a-c, the increase in V_{DC} provokes two tunability-regimes where the natural frequency either decreases or increases as shown in (i) and (ii), respectively. The voltage V_{Meas} measured by the optical detection apparatus is proportional to the steady-state displacement of the resonator. The plots only show the response in a forward (increasing) sweep of the frequency $\Omega = 2\pi f_{ext}$ of the applied $V_{RF}(t) = V_{amp}\cos(2\pi f_{ext} t)$. The voltage unit V_p denotes that the RF voltages are reported using their peak (amplitude) values. All the displayed responses are recorded for $V_{amp} =$ 3.16 mV_p, except for $V_{DC} = 5$ V in Fig. 3a,c where $V_{amp} = 10$ mV_p.

$$\delta_B(T) = \beta_0 + \beta_1 T + \beta_2 T^2, \tag{4b}$$

where the coefficients θ_0, θ_1, β_0, β_1, and β_2 are independent of temperature and voltage. These coefficients are dictated by the structural properties of the resonator (e.g., geometry and material) and the fabrication-residual stresses.

To account for the electrostatic force, we assume that m in the ROM experiences a voltage drop $V(t) = V_{DC} - V_{RF}(t)$ between the gold terminals and the Si ground (cf. Fig. 2b). As further detailed in supplemental material section S3, the nondimensional resultant force exerted on m writes

$$\overline{F}_{ext}(\overline{u}; T, V) = -\left\{ \overline{u} - \delta_B(T) + \kappa_T \overline{u} \left[1 - \overline{d}_T \frac{1 + \delta_T(T)}{\sqrt{\overline{d}_T{}^2 + \overline{u}^2}} \right] + \frac{\gamma_0 + \gamma_1 \overline{u}}{(\overline{d}_E + \overline{u})^2} V^2 \right\}, \tag{5}$$

where $\overline{u} \overset{\text{def}}{=} \frac{u}{d_B}$, $\overline{d}_T \overset{\text{def}}{=} \frac{d_T}{d_B}$, $\kappa_T \overset{\text{def}}{=} \frac{k_T}{k_B}$, $\overline{d}_E \overset{\text{def}}{=} \frac{d_E}{d_B}$, and $\{\gamma_0, \gamma_1\}$ are constants related to electrostatic force (cf. supplemental material section S3). Note that the nondimensionalization in (5) reduces the number of involved parameters in the ROM by two, namely, the reference distance d_B and stiffness k_B.

Recall that in the experiments, we impose the temperature T of the resonator and the DC voltage V_{DC}, and then we study the effect of these conditions on the vibration of the resonator as depicted in Fig. 3. Alternatively in the ROM, we can identify the effect of T and V_{DC} using (5) by computing the equilibrium normalized displacement $\overline{u}_{EQM}(T, V_{DC})$ that sets $\overline{F}_{ext}$ to zero when $V = V_{DC}$ (i.e., imposing Newton's first law). We study the vibrations about $\overline{u}_{EQM}(T, V_{DC})$ by perturbing the DC equilibrium via a weak RF voltage such that ${V_{RF}}^2 \ll 2V_{RF}V_{DC}$, which is consistent with our measurements, where the maximum RF voltage is 0.316 V_p (peak value) the smallest DC voltage is 5 V.

With $w(t; T, V_{DC} + V_{RF}(t)) \overset{\text{def}}{=} u(t; T, V_{DC} + V_{RF}(t)) - u_{EQM}(T, V_{DC})$ and $\overline{w} \overset{\text{def}}{=} \frac{w}{d_B}$, we approximate the dynamics to the order $\mathscr{O}(\overline{w}^5)$ by

$$\frac{d^2\overline{w}}{d\tau^2} + \kappa_1 \overline{w} + \kappa_2 \overline{w}^2 + \left(\kappa_3 + \kappa_3^B\right)\overline{w}^3 + \kappa_4 \overline{w}^4 + \kappa_5 \overline{w}^5 = \underbrace{-2 \frac{\gamma_0 + \gamma_1 \overline{u}_{EQM}}{(\overline{d}_E + \overline{u}_{EQM})^2} V_{DC} V_{amp} \sin\left(\frac{\Omega}{\omega_B}\tau\right)}_{\overline{F}_{RF}(t)} \tag{6}$$

according to the detailed derivation in supplemental material section S3. In (6), $\tau \overset{\text{def}}{=} \omega_B t$ is the nondimensional time coordinate where t is the dimensional time coordinate, and $\omega_B \overset{\text{def}}{=} \sqrt{\frac{k_B}{m}}$. In (6), κ_n for $n \in \{1, 2, 3, 4, 5\}$ are deduced by Taylor series expansion of $\overline{F}_{DC}(\overline{u}) \overset{\text{def}}{=} -\overline{F}_{ext}(\overline{u}; T, V_{DC})$, leading to $\kappa_n \overset{\text{def}}{=} \frac{1}{n!} \frac{d^n \overline{F}_{DC}}{d\overline{u}^n}\Big|_{\overline{u}=\overline{u}_{EQM}}$. κ_3^B in (6) represents the geometric nonlinearity of the bending response. Equation (6) assumes the RF voltage to be of the form $V_{RF}(t) = V_{amp}\sin(\Omega t)$ with frequency and amplitude Ω ${V_{amp}}^2 \ll 2V_{amp}V_{DC}$. Note that (6) does not incorporate damping because we focus on the detuning and the nonlinearity of the (natural) frequency response of the resonator.

To this end, the frequency detuning along the backbone curve of the forced response is expressed as,

$$\frac{\sigma}{\omega_B} = \frac{3}{8\sqrt{\kappa_1}} \left(\kappa_3^B + \underbrace{\kappa_3 - \frac{10}{9}\frac{\kappa_2^2}{\kappa_1}}_{\kappa_3^{T+E}} \right) \overline{w}_{amp}^2 + \left(-\frac{7}{8}\frac{\kappa_2\kappa_4}{\sqrt{\kappa_1^3}} + \frac{5}{16}\frac{\kappa_5}{\sqrt{\kappa_1}} \right) \overline{w}_{amp}^4, \tag{7}$$

where we denote by $\sigma \overset{\text{def}}{=} \omega_{Peak} - \sqrt{\kappa_1}$ the shift in peak-frequency between the nonlinear and the linear systems, by $\overline{w}_{amp}$ the amplitude of steady-state oscillations, and by κ_3^{T+E} the effective cubic nonlinearity resulting from the stretching and the electrostatic effects in the ROM of Fig. 2c. Thus, for a stiffening-to-softening behavior (exhibited in Fig. 5e and 5b), the coefficient of ${\overline{w}_{amp}}^2$ in (7) must be positive to stiffen the response at moderate amplitudes, and the coefficient of ${\overline{w}_{amp}}^4$ must be negative to soften the response at strong amplitudes, whence the decision to approximate to the quintic order of $\overline{w}$ (i.e., $\mathscr{O}(\overline{w}^5)$) [34].

3. Electrostatic frequency tuning mediated by thermoelastic buckling

In Fig. 3, we explore the relative contributions of temperature and electrostatic forces on the tuning of the linear response of the drumhead resonators. Fig. 3a, 2b, and 2c show the linear frequency response for low drive amplitudes V_{RF} gathered from the same resonator for increasing values of V_{DC} at 340 K, 320 K, and 295 K, respectively. In Fig. 3, the recorded V_{Meas} corresponds to the peak value of the amplitude of RF voltage measured by the photodetector depicted in Fig. 2b. The V_{Meas} is proportional to the steady-state amplitude of oscillation w_{amp} of the resonator via a constant labeled α (i.e., $w_{amp} = \alpha V_{Meas}$) based the employed Fabry-Pérot interferometry detection scheme (cf. supplemental material section S1.b). We note that α sensitively depends on the interferometric gap size and will be different for different values of temperature and V_{DC}.

The measurements in Fig. 3 reveal that the temperatures and DC voltage drastically affect the natural frequency of the resonator. For instance, at all temperatures of Fig. 3, the natural frequency presents two regimes of tunability with increasing V_{DC}. In the first regime of increasing V_{DC}, subfigures (i) at each temperature, the natural frequency of the resonator *decreases*, whereas in the second regime of increasing V_{DC}, in the subfigures (ii), the natural frequency *increases*.

To further highlight and observe the tunability, Fig. 4a plots the natural frequency of the resonator versus V_{DC} at 370 K, 360 K, 340 K, 320 K, and 295 K. The experimentally measured values are represented as points, while the lines indicate the trends predicted by the proposed ROM. The natural frequency at all these temperatures exhibits the two mentioned regimes of tunability with V_{DC}, which manifest in an experimental local minimum for each temperature value except for 370 K. However, this tunability with V_{DC} becomes stronger at smaller temperatures for the measured resonator, as demonstrated by the sharp minimum frequency cusp. We observe that the natural frequency exhibits an increase from 7.2 MHz for $V_{DC} = 2.5$ V to 9.9 MHz for $V_{DC} = 15$ V at 370 K ($\sim$1.3 $\times$ increase) versus an increase from 4.7 MHz for $V_{DC} = 17.5$ V to 11.3 MHz for $V_{DC} = 5$ V at 295 K ($\sim$2.4 $\times$ increase). This large tunability observed at smaller temperatures (e.g., at 295 K and 320 K in Fig. 4a) is repeatable and observed in additional resonators fabricated as shown in the supplemental material section S2 and Fig. S2-S13.

The large tunability of natural frequency is known to be caused by buckling of the drumhead resonator [52,34,27]. To validate this conjecture, we compare the experimental results of Fig. 4a with the predictions of the buckling ROM in Fig. 2c. Therefore, we assign the ROM parameters the values listed in Table 2 from the system-identification algorithm explained in the supplemental material section S4. The solid lines in Fig. 4a show the natural frequencies estimated from the ROM for different values of (T, V_{DC}). By inspecting Fig. 4a, we conclude that the ROM accurately captures the tunability of the natural frequency as a function of (T, V_{DC}) with a relative total error<5.5 % (cf. supplemental material section S4 for the error definition). We emphasize that these good predictions result from the ROM with parameters independent of the applied temperature and DC voltage (cf. Table 2). Therefore, the proposed ROM is universal to the applied (temperature, voltage) conditions for the investigated resonator.

For instance, the parameters of the ROM (cf. Table 2) depend on the geometry/material of the resonator and the residual stresses from fabrication. These effects lead to larger compressive strains at cooler temperatures as shown by the coefficients of δ_T and δ_B in Table 2. In essence, δ_T and δ_B monotonically increase (from 0.40 and 0.046 to 0.72 and 0.73, respectively) with the decrease in temperature from 370 K to 295 K (cf. supplemental material Fig. S14a-b). Hence, the ROM indicates that the strong compression in the zero-Volts-state enables the large frequency 2.4$\times$ tunability with V_{DC} exhibited in Fig. 4a. Starting from the equilibrium induced by the compressions in the zero-Volts-state, the applied decreases the effective stiffness of the resonator, thus the natural frequency, up to a local minimum (e.g., the decrease in frequency when V_{DC} goes from 4 V to $\sim$ 17.4 V at 295 K in Fig. 4a). This point of minimum frequency is referred to as the *point of critical buckling* where the structure presents the lowest stiffness due to weak stability [54]. Past the critical buckling value, the applied V_{DC} starts to stretch the resonator, which stabilizes and stiffens the resonator (e.g., the increase in frequency for $V_{DC} > 17.4V$ at 295 K in Fig. 4a).

Remarkably, the smaller temperatures in Fig. 4a not only soften the resonator but also increase its sensitivity to DC voltage. The amplified sensitivity manifests in the abrupt frequency transition around critical buckling at 295 K (i.e., discontinuous slopes). Such abrupt frequency transitions are typically observed in structures with symmetric cross-sections, which are perfectly compliant (i.e., zero natural frequency) at the critical buckling value [54,36,29]. Nonetheless, the resonators in this work do not possess symmetric cross-sections (cf. Fig. 2b) and still display the non-smooth frequency-detuning with buckling (cf. Fig. 4a and supplemental material Fig. S2), which enhances the tunability. Therefore, the experiments and the model prove that non-smooth critical buckling can be achieved even in asymmetric structures, resulting in large tunability of the natural frequency.

To highlight the high sensitivity of the dynamics to the resonator's geometry as function of the critical buckling, we use the ROM to

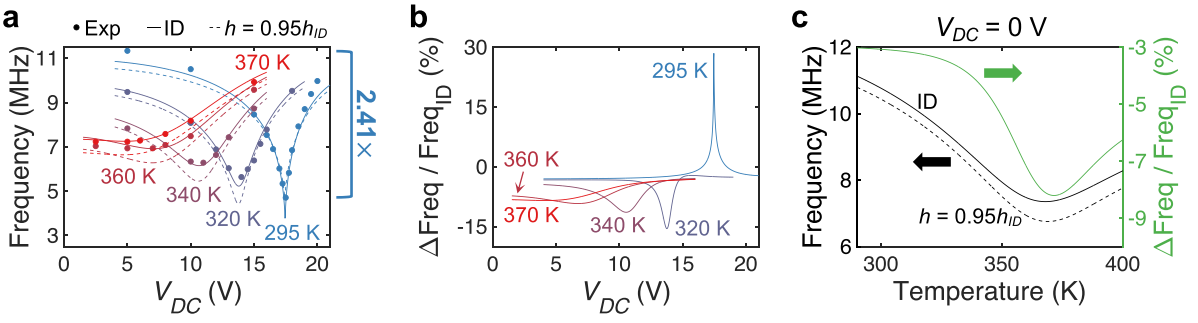

Fig. 4. Large electro-thermoelastic tunability of the resonator's natural frequency. (a) The natural frequency of the resonator as a function of the applied V_{DC} for five different temperatures. The round scatters correspond to the experimental values deduced from the linear frequency responses at $V_{amp} = 3.16$ mV$_p$, like in Fig. 3; the curves correspond to the natural frequency values reconstructed using the ROM with the identified parameters of TABLE II (solid curves) and the parameters of a hypothetical resonator with 5 % thinner resonator (dashed curves). (b) Relative change in the natural frequency predicted by the ROM due to the 5 % thickness reduction as a function of V_{DC} for the five different temperatures. (c) Natural frequency predicted by the ROM for $V_{DC} = 0$ V of the identified resonator of TABLE II (solid black curve) and the hypothetical 5 % thinner resonator (black dashed curve) as a function of temperature (left y-axis). Relative change in the natural frequency predicted by the ROM due to the 5 % thickness reduction as a function of temperature for $V_{DC} = 0$ V (right y-axis).

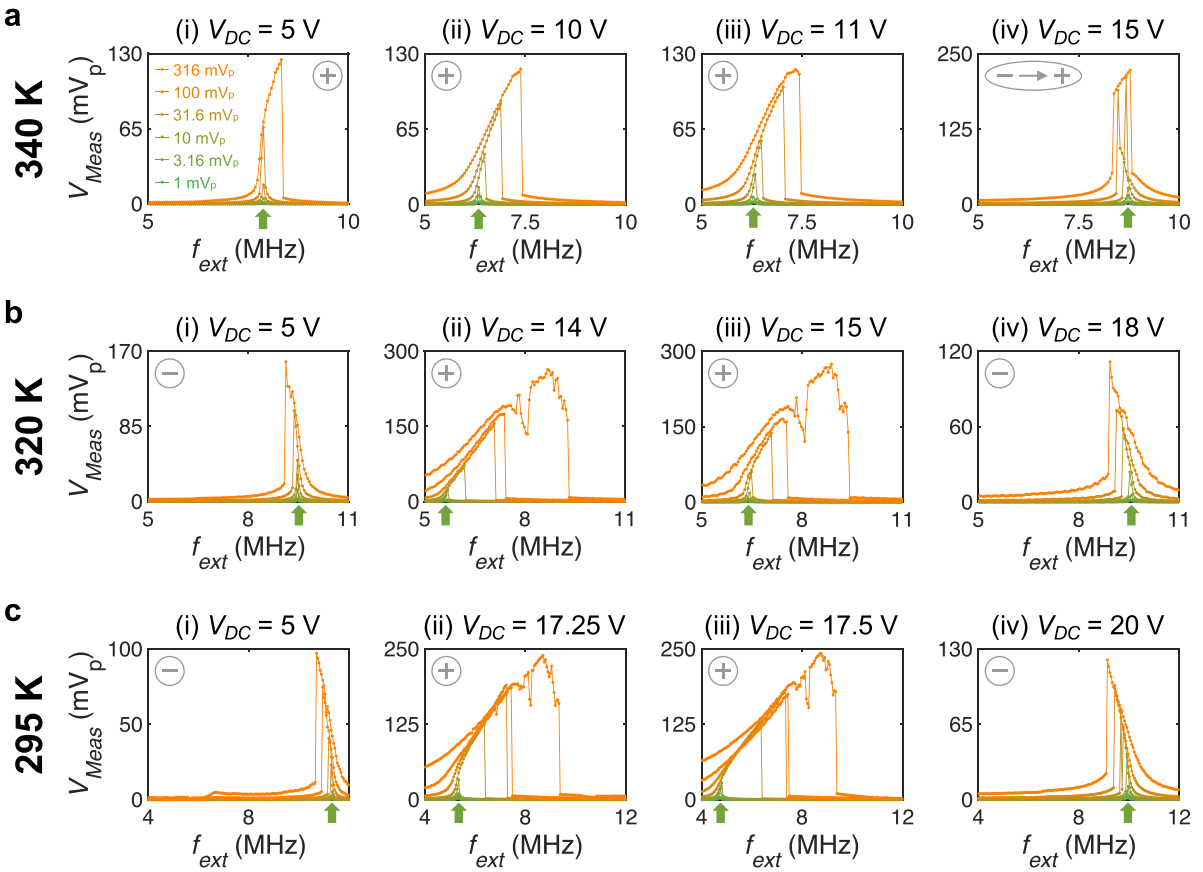

Fig. 5. Electrostatic and thermoelastic tunability of the resonator's nonlinear dynamic response. Experimentally measured frequency response of the resonator at a temperature of (a) 340 K, (b) 320 K, and (c) 295 K for increasing values of V_{DC} (from (i) to (iv)) and V_{RF} (from 1 mV_p to 316 mV_p amplitudes – cf. legend in 2a-i). The voltage V_{Meas} measured by the optical detection apparatus is proportional to the steady-state displacement of the resonator. The plots only show the response in a forward (increasing) sweep of the frequency f_{ext} of the applied $V_{RF}(t) = V_{amp}\cos(2\pi f_{ext}t)$. The voltage unit V_p denotes that the RF voltages are reported using their peak (amplitude) values. The vertical upward arrows point to the linear-resonance frequency at $V_{amp} = 3.16$ mV_p, representing the resonator's natural frequency plotted in Fig. 4a. The encircled label in the corner of each subfigure indicates the type of nonlinearity observed at the respective (T, V_{DC}) where we refer by "−" a softening nonlinearity, "+" a stiffening nonlinearity, and "−→+" a softening-to-stiffening nonlinearity.

Table 2
Identified parameters of the ROM in Fig. 2c to fit the experimental results in Fig. 4a for all temperatures and DC voltages with $\kappa_T = 1$, $\bar{d}_T = 1$, and $\bar{d}_E = 10$. Refer to (1)-(5) for the definition of the ROM nondimensional parameters. Refer to the supplemental material section S4 for details about the identification algorithm.

$\frac{\omega_B}{2\pi}$[MHz]	δ_T		δ_B			Electrostatic	
	θ_0	θ_1[K^{-1}]	β_0	β_1[K^{-1}]	β_2[K^{-2}]	γ_0[V^{-2}]	γ_1[V^{-2}]
9.40	1.9	−4.07E-3	7.65	−3.47E-2	3.81E-5	2.42E-1	−4.76E-2

examine the effect of a 5 % reduction in the thickness of the resonator. By referring to the thickness of the identified resonator in Table 2 as h_{ID}, we express a 5 % reduced thickness as $h = 0.95h_{ID}$. We assume that the thickness h affects only the mass m, the stiffnesses k_B and k_T in the ROM of Fig. 2c according to the relationships found in the literature [55,34,56] (cf. supplemental material section S5.c for a detailed explanation). These relationships affect the normalized parameters of the ROM listed in Table 2 as follows,

$$\frac{\omega_B}{\omega_{B,ID}} = \frac{h}{h_{ID}} \tag{8a}$$

$$\frac{\kappa_T}{\kappa_{T,ID}} = \left(\frac{h}{h_{ID}}\right)^{-2} \tag{8b}$$

where the "*ID*" subscript denotes the parameter of the identified resonator of thickness h_{ID}, and the parameters ω_B and κ_T characterize the resonator with varied thickness h.

In Fig. 4a, we overlay the estimated frequencies for the case $h = 0.95\,h_{ID}$, using the scaling of eq.(8). By comparing the solid line (ID) to the dashed line (0.95 ID), we observe that the effect of the thickness variation on the natural frequency is highly dependent on the temperature and voltage of the resonator. This dependence is better visualized in Fig. 4b where we plot the deviation in natural frequency Δ Freq relative to the natural frequency of the identified resonators Freq_{ID}. Fig. 4b demonstrates that the magnitude of frequency-deviations diverges close to the critical buckling of each temperature and is larger for the temperatures where the strongest frequency-tunability can be realized. For example, we see a maximum deviation in frequency of −8.5 % at 370 K vs + 28.4 % at 295 K for the same 5 % thickness variation. Hence, a small deviation in parameters of the resonator (like thickness) can strongly affect the vibrations when operating close to the critical buckling. This effect was experimentally and numerically observed in [42] where buckling transition amplifies very small deviations ($\leq$ 5 %) between the unit-resonators in nano-phononic waveguides to the extent of breaking the periodicity of the waveguides and eliminating the acoustic transmission. Note that the scaling (8) ignores the effect of thickness on the residual strain parameters (δ_T and δ_B) and their temperature-related coefficients (i.e., θ_0, θ_1, β_0, β_1, and β_2). Due to this assumption, the critical buckling occurs around the same V_{DC} for each temperature in the ROM resonators with both thicknesses h_{ID} and 0.95 h_{ID} as depicted in Fig. 4a. Though, if thickness affects the temperature-related coefficients then the thickness-variations might induce shifts in the value V_{DC} of critical buckling in Fig. 4a, which results in larger frequency-deviations in Fig. 4b.

From the experimental data in Fig. 4a (and the supplemental material Fig. S2), we conclude that achieving the ultra-tunability (e.g., at 320 K and 295 K) requires a buckling state that is determined by a combination of temperature and voltage effects. For instance, varying the temperature without applying a DC voltage (i.e., $V_{DC} = 0$ V) does not induce a sharp frequency transition as can be predicted by the low V_{DC} data for each temperature value in Fig. 4a. To clarify this behavior, we use the ROM to estimate the frequency of the resonators with thicknesses h_{ID} and 0.95 h_{ID} as a function of temperature in the absence of DC voltage as shown in Fig. 4c. Indeed, the frequency of the resonators in Fig. 4c tunes smoothly with temperature for $V_{DC} = 0$ V exhibiting a maximum increase of 1.53 × and 1.60 × for the resonators with h_{ID} and 0.95 h_{ID}, respectively, between 295 K and 370 K. This smooth frequency-tunability realizes a maximum frequency-deviation of −8.2 % between the two resonators for the temperature range in Fig. 4c.

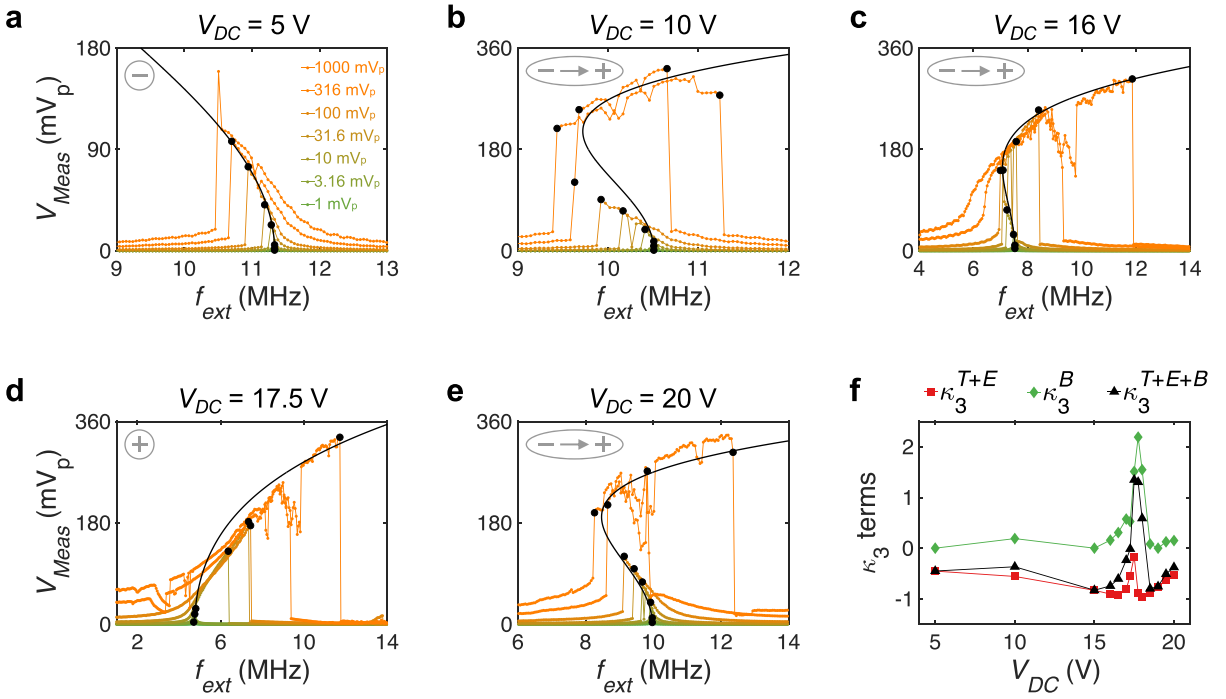

Fig. 6. Electrostatic tunability of the nonlinear response. Experimental frequency response of the resonator at 295 K for V_{DC} of (a) 5 V, (b) 10 V, (c) 16 V, (d) 17.5 V, and (e) 20 V and increasing values of V_{amp} (from 1 mV_p to 1000 mV_p amplitudes – cf. legend in 4a). Black round scatters correspond to the backbone-curve experimental datapoints used to identify κ_3^B and $\alpha \overset{\text{def}}{=} \frac{\overline{w}_{amp}}{V_{Meas}}$ to reconstruct based on (7) the nonlinear backbone-curves depicted by the solid black lines. The same assumptions and protocols stated in Fig. 3 apply to Fig. 5a-e. The encircled labels in the corner of Fig. 5a-e indicate the type of nonlinearity where we refer by "−" a softening nonlinearity, "+ " a stiffening nonlinearity, and "−→ + " a softening-to-stiffening nonlinearity. (f) Cubic nonlinear stiffness normalized terms κ_3 identified in the ROM by the resonator stretching and the electrostatic force κ_3^{T+E} (red squares), by the resonator bending κ_3^B (green diamonds), and by all the effects $\kappa_3^{T+E+B} = \kappa_3^{T+E} + \kappa_3^B$ (black triangles) as a function of the applied V_{DC}. (For interpretation of the references to colour in this figure legend, the reader is referred to the web version of this article.)

4. Switching nonlinearity with buckling

Fig. 5a-c show the nonlinear frequency response of the resonator at 340 K, 320 K, and 295 K, respectively. We note that the voltage and temperature not only vary the resonator's natural frequency but also switch the type of nonlinearity in the response. In Fig. 5a at 370 K, for larger oscillation amplitudes, the nonlinear response exhibits stiffening for $V_{DC} = 5$, 10, and 11 V in Fig. 5a(i)-(iii), respectively, but a softening-to-stiffening behavior for $V_{DC} = 15$ V in Fig. 5a(iv). We also observe a switch in nonlinear behavior with V_{DC} at 320 K and 295 K in Fig. 5b-c, where the frequency response shows softening in Fig. 5b(i) and 4c(i) for small V_{DC}, stiffening in Fig. 5b(ii)-(iii) and 4c(ii)-(iii) for V_{DC} around the critical buckling transition (cf. Fig. 4a), and finally softening in Fig. 5b(iv) and 4c(iv) for strong V_{DC}.

By comparing this switching of nonlinear response in Fig. 5 with the frequency-detuning in Fig. 4a at 370 K, 320 K, and 295 K, we conclude that the nonlinearity is stiffening close to the critical buckling point where the resonator exhibits its softest dynamics due to the applied V_{DC} at the respective temperature. We also observe that the nonlinearity is of softening type far from the critical buckling conditions. This switching trend is clear at 295 K and 320 K where we observe sharp critical buckling points in Fig. 4a, and for 370 K where the natural frequency increases rapidly for $V_{DC} > 11$ V. To summarize, the thermoelastic and electrostatic loads induce *stiffening nonlinearity when the resonator is soft* (i.e., close to the critical buckling point), and *softening nonlinearity when the resonator is stiff* (i.e., away from critical buckling). Moreover, the electrostatic-mediated thermoelastic loads result in a softening-to-stiffening nonlinearity when the resonator is not very far away from critical buckling as seen at 370 K for $V_{DC} = 15$ V in Fig. 5a(iv). We observe this same nonlinearity switching around critical buckling for different resonators at different temperatures and DC voltages as illustrated in the supplemental material Fig. S2-S13 and later in Fig. 6 at 295 K.

To explain the physics governing the switching in nonlinearity, we study in Fig. 6 the nonlinear response at 295 K using the ROM of Fig. 2c. We apply (7) to estimate the backbone-curve of the nonlinear frequency response with the parameters of the identified resonator listed in Table 2. These parameters compute every coefficient in (7) except for the nonlinear bending-term, and the proportionality α relating $\overline{w}_{amp} = \alpha V_{Meas}$ at each temperature T and DC voltage V_{DC}. Thus, we identify κ_3^B and α for each V_{DC} at 295 K by fitting (7) with $\overline{w}_{amp} = \alpha V_{Meas}$ to the experimental backbone-curve points depicted in Fig. 6a-e. We select these backbone-curve points by choosing the datapoints with maximum amplitude in the continuous responses (i.e., linear responses) and the datapoints at jumps (sudden transitions) in the discontinuous responses (i.e., nonlinear responses).

We plot in Fig. 6f the identified values of κ_3^B, which reconstructs according to (7) the nonlinear backbone-curves depicted as solid-black lines in Fig. 6a-e. We see that the model captures, (i) the softening nonlinearity away from critical-buckling for $V_{DC} = 5$ V in Fig. 6a, (ii) the softening-to-stiffening nonlinearity around critical-buckling for $V_{DC} = 10$ V, 16 V, and 20 V in Fig. 6b, 5c, and 5e, respectively, and lastly (iii) the stiffening nonlinearity very-close to critical-buckling for $V_{DC} = 17.5$ V in Fig. 6d (cf. Fig. 4a to locate critical-buckling as a function of V_{DC} at 295 K). It is interesting that the model (7) captures this switching in nonlinearity not only qualitatively but also quantitatively by estimating very well the nonlinear frequency-detuning as depicted in Fig. 6a-e (except for $V_{DC} = 10$ V in Fig. 6b where we see some deviation between the experiments and the modeled backbone-curve). Therefore, the ROM in Fig. 2c with the introduced bending nonlinearity κ_3^B can accurately model and predict the nonlinear response of the resonator under thermo-electric buckling.

To explain the physical mechanism of the switching in nonlinearity, we plot in Fig. 6f the effective cubic nonlinear coefficient κ_3^{T+E} induced by stretching and electrostatic effects in addition to κ_3^B induced by the bending geometric effect. We investigate the effective cubic nonlinear coefficients (i.e., quadratic, and cubic coefficients) since they govern the nonlinear response for small to moderate amplitudes as dictated by (7). We observe in Fig. 6f that for all the measured values of V_{DC} at 295 K, κ_3^{T+E} is negative whereas κ_3^B is positive. Hence, the *stretching and electrostatic effects induce softening nonlinearity*, but the *bending geometric effect induces stiffening nonlinearity*.

Finding κ_3^B to be positive aligns with its definition of representing the geometric stiffening of bending. The negative κ_3^{T+E} indicates that the softening nonlinearity results from the electrostatic and stretching effects. An electrostatic softening effect conforms with the nature of the capacitive force in (5). As for the softening effect of the stretching force, we emphasize that the stretching spring is compressed at equilibrium given that $\delta_T > 0$, as shown by (4), Table 2, and supplement figure S14. Due this compression, the stretching of the resonator can induce softening effects. For example, in the case of an equilibrium at $\overline{u}_{EQM} = 0$, the displacements elongate the stretching spring until fully relaxed at a deformed length $\sqrt{{d_T}^2 + u^2}$ equal to the spring free length L_T (cf. Fig. 2c). In this scenario, the force in the stretching spring decreased until vanishing with the increased displacement, thus the softening nonlinearity. For the other cases of $\delta_T > 0$ where $\overline{u}_{EQM} \neq 0$ (i.e., $\overline{u}_{EQM} > 0$ because also $\delta_B > 0$), similar relaxation of the stretching spring occurs with displacements increasing in one direction (i.e., in the positive direction of $\overline{u}_{EQM}$) but not the other, leading to softening (asymmetric) nonlinearity. These nonlinear effects explained at the ROM level can be translated to the physical resonator thanks to the physics-based approach adopted in the ROM derivation.

Moreover, Fig. 6f demonstrates that the stretching and electrostatic effects dominate the total effective cubic nonlinearity κ_3^{T+E+B} away from critical buckling (for $V_{DC} \leq 17.25$ V and $V_{DC} \geq 18.5$ V) while the bending geometric effect dominates κ_3^{T+E+B} close to critical buckling (for $V_{DC} \in [17.5\text{ V}, 18\text{ V}]$). Therefore, the dominance of bending geometric effects at critical buckling drives the switching in nonlinearity from softening to stiffening as the resonator becomes closer to critical buckling in the experiments of Fig. 5, 6a-e, and the supplemental material, cf. Figs. S3-S13. From Fig. 6f, we can also conclude that the stiffening nonlinearity around the critical buckling is (~2 times) stronger than the softening nonlinearity away from the critical buckling. This increase in nonlinearity around critical buckling explains the strong nonlinear frequency-detuning demonstrated by the stiffening response in Fig. 5b(ii)-(iii), c(ii)-(iii), and

Fig. 6d.

5. Discussion of the ROM

This ROM serves in modeling the investigated resonators due to its geometry agnosticism. In other words, to apply the ROM, we don't need to know the geometry of the different constituents in the resonators. This property is highly needed for the investigated resonators because they are formed of multiple layers with nonuniform cross-sections [42]. Thanks to this ROM, this work is the first, up to the authors' knowledge, to study buckling in irregular MEMS/NEMS structures. For instance, existing studies treat buckled microresonators by continuum modeling that applies to beams [26,27,31,34,40,41,36] and plates of perfectly rectangular [53,57] and circular [32,55] shapes.

However, the continuum modeling allows computing the stresses in the material [27,34,36,53,55], which our developed ROM can't estimate. Nonetheless, we anticipate that this ROM will find important utility in assisting current analytical [55,58], numerical [59,60,52], and empirical [53,61] methods that predict the behavior of MEMS structures. In particular, this ROM reduces the degrees of freedom while capturing the essential governing dynamic mechanisms, thus accelerating the design and prototyping processes [59].

6. Conclusions

In this work, we experimentally study the electrostatically-mediated thermoelastic tunability of micro-drumhead resonators. We show that these drumhead resonators with high compressive strains – introduced by cooling – present large tunability of their natural frequency with DC voltage. We also find that DC voltage switches the nonlinear response of the resonator by regulating its state of buckling. For instance, the resonators show stiffening nonlinearity, with stronger nonlinear frequency-detuning, close to the critical buckling, while the nonlinearity is of softening type as the resonator moves away from the critical buckling point. We formulated and identified the parameters of a reduced order model (ROM) that captures the experimental linear and nonlinear dynamics for different temperatures and DC voltages. The developed reduced order model is based on lumped mass-springs representations, which is valuable in designing and studying buckled metamaterials and phononic waveguides. Thanks to this ROM, we demonstrate that the geometric bending effect induces stiffening nonlinearity, whereas the electrostatic and softening effects induce softening nonlinearity. Moreover, the ROM highlights the importance of compression to achieve softening nonlinearity.

Indeed, buckling can be exploited to enable new and unusual capabilities in tuning and designing resonators in MEMS. Moreover, the buckling effect can be regulated via electric voltage, which is easily integrated in devices and systems. In this study, optimal buckling performance also required thermal control, which cannot be deployed easily in standalone systems. In the future, additional work should be conducted to design the resonators such that the electric control of buckling leads to ultra-fine tunability at the desired temperature of operation, such as room temperature. Such work requires unraveling the relationship between the structure's mechanics, the strains (e.g., δ_T and δ_B), temperature, and fabrication-residual stresses. Hence, additional experimental, numerical, and analytical work should be conducted to benefit from buckling for vibrations in NEMS.

Declaration of Competing Interest

The authors declare that they have no known competing financial interests or personal relationships that could have appeared to influence the work reported in this paper.

Data availability

Data will be made available on request.

Acknowledgement

This work was supported in part by the NSF Emerging Frontiers in Research and Innovation (EFRI) Grant 1741565. P.F. and A.M.v.d.Z acknowledge the support of the NSF-CAREER Award number CMMI-184673.

Appendix A. Supplementary data

Supplementary data to this article can be found online at https://doi.org/10.1016/j.ymssp.2023.110331.

References

[1] Y. Shim, Z. Wu, M. Rais-Zadeh, A high-performance continuously tunable MEMS bandpass filter at 1 GHz, IEEE Trans. Microw. Theory Tech. 60 (8) (2012) 2439–2447.
[2] L. Ma, N. Soin, M.H.M. Daut, S.F.W.M. Hatta, Comprehensive study on RF-MEMS switches used for 5G scenario, IEEE Access 7 (2019) 107506–107522.
[3] S.-G. Kim, S. Priya, I. Kanno, Piezoelectric MEMS for energy harvesting, MRS Bull. 37 (11) (2012) 1039–1050.

[4] T. Gebrael, A. Kanj, D. Farhat, M. Shehadeh, I. Lakkis, Self sustained thermally induced gas-damped oscillations of bimetal cantilevers with application to the design of a new pyroelectric micro energy harvester, J. Phys. D Appl. Phys. 53 (19) (2020), 195501.
[5] H. Liu, Y. Qian, C. Lee, A multi-frequency vibration-based MEMS electromagnetic energy harvesting device, Sens. Actuators, A 204 (2013) 37–43.
[6] M. Li, H.X. Tang, M.L. Roukes, Ultra-sensitive NEMS-based cantilevers for sensing, scanned probe and very high-frequency applications, Nat. Nanotechnol. 2 (2) (2007) 114–120.
[7] N. Kacem, S. Hentz, D. Pinto, B. Reig, V. Nguyen, Nonlinear dynamics of nanomechanical beam resonators: improving the performance of NEMS-based sensors, Nanotechnology 20 (27) (2009), 275501.
[8] E.A. Kittlaus, W.M. Jones, P.T. Rakich, N.T. Otterstrom, R.E. Muller, M. Rais-Zadeh, Electrically driven acousto-optics and broadband non-reciprocity in silicon photonics, Nat. Photonics 15 (1) (2021) 43–52.
[9] A.H. Safavi-Naeini, D. Van Thourhout, R. Baets, R. Van Laer, Controlling phonons and photons at the wavelength scale: integrated photonics meets integrated phononics, Optica 6 (2) (2019) 213–232.
[10] C. Chen, S. Rosenblatt, K.I. Bolotin, W. Kalb, P.a.K.I. Kim, H.L. Stormer, T.F. Heinz, J. Hone, Performance of monolayer graphene nanomechanical resonators with electrical readout, Nat. Nanotechnol. 4 (12) (2009) 861–867.
[11] P. Weber, J. Guttinger, I. Tsioutsios, D.E. Chang, A. Bachtold, Coupling graphene mechanical resonators to superconducting microwave cavities, Nano Lett. 14 (5) (2014) 2854–2860.
[12] M. Merklein, B. Stiller, K. Vu, S.J. Madden, B.J. Eggleton, A chip-integrated coherent photonic-phononic memory, Nature Communications 8 (1) (2017) 1–7.
[13] H. Shin, J.A. Cox, R. Jarecki, A. Starbuck, Z. Wang, P.T. Rakich, Control of coherent information via on-chip photonic–phononic emitter–receivers, Nat. Commun. 6 (1) (2015) 1–8.
[14] E. Verhagen, S. Deleglise, S. Weis, A. Schliesser, T.J. Kippenberg, Quantum-coherent coupling of a mechanical oscillator to an optical cavity mode, Nature 482 (7383) (2012) 63–67.
[15] R.W. Andrews, R.W. Peterson, T.P. Purdy, K. Cicak, R.W. Simmonds, C.A. Regal, K.W. Lehnert, Bidirectional and efficient conversion between microwave and optical light, Nat. Phys. 10 (4) (2014) 321–326.
[16] D. Hatanaka, I. Mahboob, K. Onomitsu, H. Yamaguchi, Phonon waveguides for electromechanical circuits, Nat. Nanotechnol. 9 (7) (2014) 520–524.
[17] W. Fu, Z. Shen, Y. Xu, C.-L. Zou, R. Cheng, X. Han, H.X. Tang, Phononic integrated circuitry and spin–orbit interaction of phonons, Nat. Commun. 10 (1) (2019) 1–7.
[18] S. Gertler, P. Kharel, E.A. Kittlaus, N.T. Otterstrom, P.T. Rakich, Shaping nonlinear optical response using nonlocal forward Brillouin interactions, New J. Phys. 22 (4) (2020), 043017.
[19] K.A. Higginson, M.A. Costolo, E.A. Rietman, Adaptive geometric optics derived from nonlinear acoustic effects, Appl. Phys. Lett. 84 (6) (2004) 843–845.
[20] M.S. Kang, A. Butsch, P.S.J. Russell, Reconfigurable light-driven opto-acoustic isolators in photonic crystal fibre, Nat. Photonics 5 (9) (2011) 549–553.
[21] J. Kim, M.C. Kuzyk, K. Han, H. Wang, G. Bahl, Non-reciprocal Brillouin scattering induced transparency, Nat. Phys. 11 (3) (2015) 275–280.
[22] C. Wang, A. Kanj, A. Mojahed, S. Tawfick, A.F. Vakakis, Experimental Landau-Zener Tunneling for Wave Redirection in Nonlinear Waveguides, Phys. Rev. Appl 14 (3) (2020), 034053.
[23] C. Wang, A. Kanj, A. Mojahed, S. Tawfick, A. Vakakis, Wave redirection, localization, and non-reciprocity in a dissipative nonlinear lattice by macroscopic Landau-Zener tunneling: Theoretical results, J. Appl. Phys. 129 (9) (2021), 095105.
[24] A. Kanj, C. Wang, A. Mojahed, A. Vakakis, S. Tawfick, Wave redirection, localization, and non-reciprocity in a dissipative nonlinear lattice by macroscopic Landau-Zener tunneling: Experimental results, AIP Adv. 11 (6) (2021), 065328.
[25] N. Hu, R. Burgueno, Buckling-induced smart applications: recent advances and trends, Smart Mater. Struct. 24 (6) (2015), 063001.
[26] N. Alcheikh, A.Z. Hajjaj, N. Jaber, M.I. Younis, Electrothermally actuated tunable clamped-guided resonant microbeams, Mech. Syst. Sig. Process. 98 (2018) 1069–1076.
[27] A.Z. Hajjaj, N. Alcheikh, A. Ramini, M.A. Al Hafiz, M.I. Younis, Highly tunable electrothermally and electrostatically actuated resonators, J. Microelectromech. Syst. 25 (3) (2016) 440–449.
[28] P. X.-L. Feng, Z. Wang, J. Lee, R. Yang, X. Zheng, K. He and J. Shan, "Two-dimensional nanoelectromechanical systems (2D NEMS) via atomically-thin semiconducting crystals vibrating at radio frequencies," *2014 IEEE International Electron Devices Meeting,* pp. 8-1, 2014.
[29] E. Kramer, J. Van Dorp, R. Van Leeuwen, W. Venstra, Strain-dependent damping in nanomechanical resonators from thin MoS2 crystals, Appl. Phys. Lett. 107 (9) (2015), 091903.
[30] D.R. Southworth, H.G. Craighead, J.M. Parpia, Pressure dependent resonant frequency of micromechanical drumhead resonators, Appl. Phys. Lett. 94 (2009), 213506.
[31] S. Rajasekaran, H.B. Khaniki, Bending, buckling and vibration of small-scale tapered beams, Int. J. Eng. Sci. 120 (2017) 172–188.
[32] L. Medina, R. Gilat, S. Krylov, Bistability criterion for electrostatically actuated initially curved micro plates, Int. J. Eng. Sci. 130 (2018) 75–92.
[33] I. Kozinsky, H.W.C. Postma, I. Bargatin, M.L. Roukes, Tuning nonlinearity, dynamic range, and frequency of nanomechanical resonators, Appl. Phys. Lett. 88 (25) (2006), 253101.
[34] C. Samanta, N. Arora, A. Naik, Tuning of geometric nonlinearity in ultrathin nanoelectromechanical systems, Appl. Phys. Lett. 113 (11) (2018), 113101.
[35] S. Manzeli, D. Dumcenco, G. Migliato Marega, A. Kis, Self-sensing, tunable monolayer MoS2 nanoelectromechanical resonators, Nat. Commun. 10 (1) (2019) 4831.
[36] Y. Zhang, S. Hosono, N. Nagai, K. Hirakawa, Effect of buckling on the thermal response of microelectromechanical beam resonators, Appl. Phys. Lett. 111 (2) (2017), 023504.
[37] S. Kim, J. Yu, A.M. Van Der Zande, Nano-electromechanical drumhead resonators from two-dimensional material bimorphs, Nano Lett. 18 (11) (2018) 6686–6695.
[38] J. Cha, C. Daraio, Electrical tuning of elastic wave propagation in nanomechanical lattices at MHz frequencies, Nat. Nanotechnol. 13 (11) (2018) 1016–1020.
[39] M. Kurosu, D. Hatanaka, H. Okamoto and H. Yamaguchi, "Buckling-induced quadratic nonlinearity in silicon phonon waveguide structures," *arXiv preprint arXiv: 2112.00909,* 2021.
[40] M. Mojahedi, Size dependent dynamic behavior of electrostatically actuated microbridges, Int. J. Eng. Sci. 111 (2017) 74–85.
[41] E. Manoach, J. Warminski, L. Kloda, A. Warminska, S. Doneva, Nonlinear vibrations of a bi-material beam under thermal and mechanical loadings, Mech. Syst. Sig. Process. 177 (2022) 109127.
[42] S. Kim, J. Bunyan, P.F. Ferrari, A. Kanj, A.F. Vakakis, A.M. Van Der Zande, S. Tawfick, Buckling-mediated phase transitions in nano-electromechanical phononic waveguides, Nano Lett. 21 (15) (2021) 6416–6424.
[43] I. Wilson-Rae, R. Barton, S. Verbridge, D. Southworth, B. Ilic, H.G. Craighead, J. Parpia, High-Q nanomechanics via destructive interference of elastic waves, Phys. Rev. Lett. 106 (4) (2011), 047205.
[44] J. Liu, K. Usami, A. Naesby, T. Bagci, E.S. Polzik, P. Lodahl, S. Stobbe, High-Q optomechanical GaAs nanomembranes, Appl. Phys. Lett. 99 (24) (2011), 243102.
[45] B. Zwickl, W. Shanks, A. Jayich, C. Yang, A.B. Jayich, J. Thompson, J. Harris, High quality mechanical and optical properties of commercial silicon nitride membranes, Appl. Phys. Lett. 92 (10) (2008), 103125.
[46] D. Hatanaka, I. Mahboob, H. Okamoto, K. Onomitsu, H. Yamaguchi, An electromechanical membrane resonator, Appl. Phys. Lett. 101 (6) (2012), 063102.
[47] J. Thompson, B. Zwickl, A. Jayich, F. Marquardt, S. Girvin, J. Harris, Strong dispersive coupling of a high-finesse cavity to a micromechanical membrane, Nature 452 (7183) (2008) 72–75.
[48] J.C. Sankey, C. Yang, B.M. Zwickl, A.M. Jayich, J.G. Harris, Strong and tunable nonlinear optomechanical coupling in a low-loss system, Nat. Phys. 6 (9) (2010) 707–712.
[49] R. Potekin, S. Kim, D.M. McFarland, L.A. Bergman, H. Cho, A.F. Vakakis, A micromechanical mass sensing method based on amplitude tracking within an ultra-wide broadband resonance, Nonlinear Dyn. 92 (2) (2018) 287–304.

[50] R. Potekin, K. Asadi, S. Kim, L.A. Bergman, A.F. Vakakis, H. Cho, Ultrabroadband microresonators with geometrically nonlinear stiffness and dissipation, Phys. Rev. Appl 13 (1) (2020), 014011.
[51] Z. Bazant, L. Cedolin, "Von Mises Truss," in *Stability of structures: elastic, inelastic, fracture and damage theories*, World Scientific, Singapore, 2010, pp. 228–231.
[52] D. Gu, H.-H. Dai, F. Xu, Buckling of an elastic layer based on implicit constitution: Incremental theory and numerical framework, Int. J. Eng. Sci. 169 (2021), 103568.
[53] V. Ziebartl, O. Paul and H. Baltes, "Extraction of the coefficient of thermal expansion of thin films from buckled membranes," *MRS Online Proceedings Library (OPL),* vol. 546, 1998.
[54] L.N. Virgin, "Highly Deformed Structures," in *Vibration of Axially-Loaded Structures*, Cambridge University Press, Cambridge, 2010, pp. 237–260.
[55] G.W. Vogl, A.H. Nayfeh, A reduced-order model for electrically actuated clamped circular plates, J. Micromech. Microeng. 15 (4) (2005) 684.
[56] S. Timoshenko, Analysis of bi-metal thermostats, Josa 11 (3) (1925) 233–255.
[57] J. Awrejcewicz, G. Sypniewska-Kaminska, O. Mazur, Analysing regular nonlinear vibrations of nano/micro plates based on the nonlocal theory and combination of reduced order modelling and multiple scale method, Mech. Syst. Sig. Process. 163 (2022), 108132.
[58] A.H. Nayfeh, M.I. Younis, E.M. Abdel-Rahman, Reduced-order models for MEMS applications, Nonlinear Dyn. 41 (1) (2005) 211–236.
[59] S.D. Senturia, N. Aluru, J. White, Simulating the behavior of MEMS devices: Computational methods and needs, Comput. Sci. Eng. 4 (1) (1997) 30–43.
[60] S. D. Senturia, "CAD challenges for microsensors, microactuators, and microsystems," *Proceedings of the IEEE,* vol. 86, no. 8, pp. 1611-1626, 1998.
[61] S. Spearing, Materials issues in microelectromechanical systems (MEMS), Acta Mater. 48 (1) (2000) 179–196.